Comparison of Theoretical Biases in Estimating Polarimetric Properties of Precipitation With Weather Radar Using Parabolic Reflector, or Planar and Cylindrical Arrays

Lei Lei, Guifu Zhang, *Senior Member, IEEE*, Richard J. Doviak, *Life Fellow, IEEE*, and Shaya Karimkashi, *Member, IEEE*

***Abstract*—Planar or cylindrical phased arrays are two candidate antennas for future polarimetric weather radar. These two candidate antennas have distinctly different attributes when used to make quantitative measurements of the polarimetric properties of precipitation. Of critical concern is meeting the required polarimetric performance for all directions of the electronically steered beam. The copolar and cross-polar radiation patterns and polarimetric parameter estimation performances of these two phased array antennas are studied and compared with that obtained using a dual-polarized parabolic reflector antenna. Results obtained from simulation show that the planar polarimetric phased array radar has unacceptable polarimetric parameter biases that require beam to beam correction, whereas biases obtained with the cylindrical polarimetric phased array radar are much lower and comparable to that obtained using the parabolic reflector antenna.**

***Index Terms*—Antenna, cylindrical array, phased array radar, planar array, polarimetry, radiation patterns, remote sensing, weather measurement.**

I. Introduction

THE USA's network of singularly polarized (i.e., linear horizontal) weather radar (i.e., the WSR-88D) has been updated to simultaneously transmit and receive vertically (i.e., the electric field lies in the vertical plane) and horizontally polarized waves of equal intensity along the beam axis (i.e., boresight). This dual-polarization capability improves rainfall rate estimation [4], [22] and provides the classification of hydrometeors (e.g., rain, hail, snow, etc. [16], [25], [32]) and nonweather objects (e.g., ground clutter, insects, birds, etc. [20], [24]). Moreover, polarimetric radar data can be used to retrieve the microphysical properties of clouds and precipitation (e.g., drop size distribution, particle size, particle shape, etc. [29]).

A multimission phased array radar (MPAR) is being considered as a future replacement to simultaneously serve the functions of weather and aircraft surveillance at a significant lifetime cost savings while providing significant improvement in weather surveillance performance. For example, a four-faced planar PAR antenna with electronic beam steering allows receptions of echoes from four sectors, and time multiplexing of radar assets allows the multimission surveillance of aircraft and weather [36]. Time multiplexing missions preserve the required update time needed to track aircraft while scanning and potentially provide faster update rates of hazardous weather. Faster update rates for the surveillance of severe storms that might spawn weather hazards can increase lead times for weather hazard warnings [37]. Moreover, more rapid volumetric scans can improve forecasts of a storm's evolution based on numerical weather prediction (NWP) models, and thus, warnings can be based on forecasts, rather than the detection of the hazard itself [7], [28]. Furthermore, an MPAR could reduce the total number of radar sites because one radar network could be used for the surveillance of both weather and aircraft [26], [27], [37], and thus, there is a potential to reduce the usage of spectrum space [34].

If an MPAR is to be used for weather observations, the weather community expects it to have a polarimetric measurement capability [i.e., to be a polarimetric phased array radar (PPAR)] that matches the performance and accuracy of the WSR-88D, but with more frequent data updates. It would be ideal for the PPAR to have, as does the WSR-88D for any beam direction, the copolar E_θ (see Fig. 1) along the boresight to be purely transmitted and received using only the V port of the antenna. Likewise, the boresight copolar E_ϕ should be purely transmitted and received using only the H port—this definition of cross-polar fields is consistent with definition 2 in [17]. This ideal condition is practically achieved with the parabolic reflector of the WSR-88D, and polarimetric parameters have been satisfactorily measured using the simultaneous transmission and simultaneous reception (STSR) mode of data collection [18].

Manuscript received August 26, 2014; revised November 24, 2014; accepted December 11, 2014.

L. Lei was with the School of Electrical and Computer Engineering, University of Oklahoma, Norman, OK 73019 USA, and also with the Advanced Radar Research Center, University of Oklahoma, Norman, OK 73019 USA. She is now with Delphi Electronics & Safety, Kokomo IN 46902-46902 USA.

G. Zhang is with the Advanced Radar Research Center and the School of Electrical and Computer Engineering, University of Oklahoma, Norman, OK, 73019 USA, and also with the School of Meteorology, University of Oklahoma, Norman, OK 73072 USA.

R. J. Doviak is with the School of Electrical and Computer Engineering, University of Oklahoma, Norman, OK 73019 USA, with the School of Meteorology, University of Oklahoma, Norman, OK 73072 USA, and also with the National Severe Storms Laboratory, National Oceanic and Atmospheric Administration (NOAA), Norman, OK 73072 USA.

S. Karimkashi is with the Advanced Radar Research Center, University of Oklahoma, Norman, OK 73019 USA.

Digital Object Identifier 10.1109/TGRS.2015.2395714

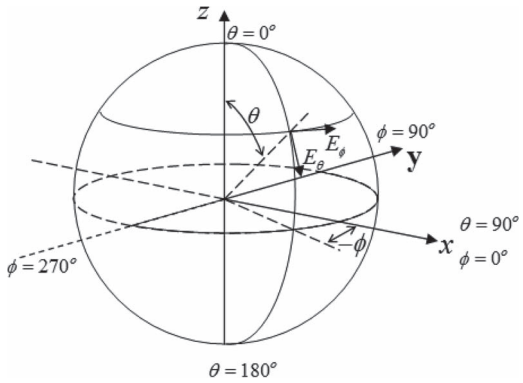

Fig. 1. Spherical coordinate system with the polar axis vertical is used to plot radiation patterns and defines variables used in this paper.

STSR and alternate transmission and simultaneous reception (ATSR) are transmission modes in which equal amplitude voltages are either simultaneously or alternately applied to the H and V antenna ports for any beam directions.

This ideal condition of the polarization orthogonally is theoretically also achieved with a cylindrical PPAR (CPPAR) in which the beam direction is always in the vertical plane bisecting the active sector (e.g., 90° [31])—azimuth scans are obtained by commuting the entire active sector by one column for each new beam azimuthal direction. A planar PPAR (PPPAR) has this property only if the array element is a pair of ideal collinear magnetic and electric dipoles [6], [14], [34].

But if the PPPAR has common H and V array elements, as do most PPPARs, this ideal property is not attained, and wanted copolar and unwanted cross-polar fields are transmitted along the boresight. That is, if the beam is electronically steered away from the cardinal planes, cross-polar beams coaxial with the copolar beam are formed as shown in Section II. Cross-polar beams coaxial with the copolar beams can create large biases as noted by Zrnić *et al.* [35]. This unwanted or geometrically induced cross-polar field cannot be ignored if it significantly biases estimates of polarimetric parameters (e.g., the Z_{DR} bias needs to be less than 0.1 dB [9]).

Corrections for each beam direction are needed to suppress biases, particularly those large biases created when the beam is steered away from the principal planes of the array, to provide the accurate quantitative measurement of the polarimetric properties of precipitation. Zhang *et al.* [30] provided bias corrections for a PPPAR consisting of crossed dipoles, and Zrnić *et al.* [33] added Doppler effects in bias corrections. These corrections apply to beams of infinitesimal width for which only the cross-polar fields along the boresight are considered in bias calculation. Lei *et al.* [15] developed bias corrections for a PPPAR consisting of an array of idealized aperture and patch elements, and again, cross-polar fields only along the boresight are considered. Zrnić *et al.* [35] and Galletti and Zrnić [12] examined cross-polar fields of a reflector antenna and assumed that copolar and cross-polar fields can be modeled by Gaussian shaped beams in which the cross-polar field over the entire angular space is used to obtain the Z_{DR}, ϕ_{dp}, and copolar correlation coefficient, ρ_{hv}, biases.

Herein, we calculate the biases of polarimetric parameter estimates (i.e., differential reflectivity Z_{DR} the magnitude of copolar correlation coefficient ρ_{hv}, and differential phase ϕ_{dp}) obtained with PPPAR and CPPAR having an array of patches and compare these biases to those incurred if an ideal center-fed parabolic reflector is used, one having the size and shape of the WSR-88D but not the narrow ridges of sidelobes due to the three feed support structures; such sidelobes are absent in the radiation from PPARs and parabolic reflectors having offset feeds [5]. Henceforth, we refer to this ideal WSR-88D simply as the WSR-88D having a diameter D of 8.54 m and an $f/D = 0.375$ (f is the focal length). Results are calculated for operation at a wavelength of 11.09 cm used by KOUN, NSSL's R&D WSR-88D, so theoretical radiation patterns can be compared with measurements. All three antennas are assumed to have identical aperture distributions. One objective of this paper is to determine angular scan limits on CPPAR and PPPAR to make polarimetric measurements with acceptable bias without beam to beam calibration while preserving the performance standards of the WSR-88D.

The differences of the WSR-88D, PPPAR, and CPPAR copolar and cross-polar radiation patterns are discussed in Section II. In Section III, the theoretical biases in the estimates of the hydrometeors' polarimetric parameters using these three antennas are calculated if no corrections are applied to remove the biases. The biases given in Section III are also compared with the results given in [15] and [30], as well as with those biases presented in [35] for an ideal center-fed parabolic reflector antenna. Conclusions and discussions are provided in Section IV.

II. Comparisons of the WSR-88D, PPPAR, and CPPAR Radiation Patterns

A. Description of the Antennas

The WSR-88D radar has a parabolic reflector antenna with a diameter of 8.54 m [see Fig. 2(a)] and a co-polar beamwidth of about 1°. If the planar array is to provide angular resolution at least as good as that of the WSR-88D for all pointing directions, each beam of the four-beam planar array (see Fig. 2(b); only one beam is shown) requires an array having an elliptical shape with a 8.54/cos(45°) meter horizontal length $2R_y$ and a 8.54 meter vertical length $2R_z$ (i.e., the azimuthal beamwidth needs to be 1° at the largest azimuth electronic scan angle of 45°, and sidelobes at angles beyond 10° need to be below −50 dB). There is a small loss of angular resolution as the elevation angle increases, but the increased beamwidth compensates for the gaps that presently exist in the elevation coverage of the WSR-88D volume scans. Each face of the PPAR electronically steers the beam ±45° in azimuth and at least 0° to 20° in elevation over which quantitative estimates of weather should nearly match or exceed that of the WSR-88D.

A four-sector CPPAR has a 8.54/cos(45°) meter diameter and a 8.54-m vertical dimension [see Fig. 2(c)]. Each 90° sector of the CPPAR generates one of four beams (one is shown) which are always azimuthally separated by 90° as the beams are synchronously steered in azimuth by commutating the aperture distributions column by column. The vertical beamwidth of the PPPAR and CPPAR increases slightly—6%—with elevation angles between 0° and 20°; it is assumed that this increase in

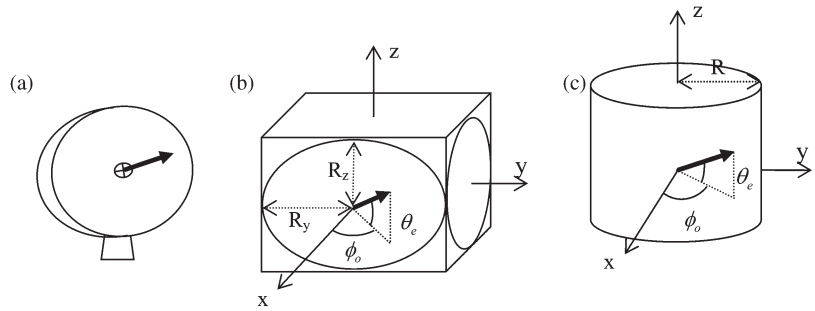

Fig. 2. (a) WSR-88D center-fed parabolic reflector, (b) four-faced planar array, and (c) four-sector cylindrical array. Single-sided bold arrows indicate beam direction.

beamwidth with elevation angle is acceptable for all MPAR functions and estimates of H and V reflectivities.

Given the distribution of the electric field across the aperture of the WSR-88D's parabolic reflector and given the far field of the array element and the weight applied to each of the elements to approximately match the radiation pattern of the WSR-88D, the theoretical far field radiation patterns can be computed for each of the radars and compared with available experimental results.

B. Aperture Distribution and Element Weightings

WSR-88D Aperture Distribution: The WSR-88D feed horn's E field is nearly axial symmetric, and the normalized electric field across the aperture is well approximated by

$$W(\rho) \simeq \frac{\left[1-(\rho/\rho_o)^2\right]^a + b}{1+b} \tag{1}$$

where $\rho_o = 4.77$ m, $a = 3$, and $b = 0.16$ [8]. This aperture distribution was computed for KOUN, a prototype dual-polarimetric WSR-88D, which used a dual-port circular feed horn having predominantly a TE_{11} electric field distribution across its aperture—this aperture field suppresses much of the cross-polar field generated by the reflector (see Appendix A and [10], section 8).

PPPAR Element Weighting: To mimic the aperture distribution of the WSR-88D [8], the amplitude weights w_{mn} applied to the mnth element of the PPPAR are

$$w_{mn} = \frac{\left[1-\left(\frac{y_n^2}{R_y^2}+\frac{z_m^2}{R_z^2}\right)\right]^a + b}{1+b} \tag{2}$$

where y_n is the horizontal distance of the nth column from the center of the elliptical array and z_m is the vertical distance of the mth row from the center row of the elliptical array. Thus, PPPAR projected aperture distribution matches that of the WSR-88D only for the beam at $\theta_o = 90^\circ$, $\phi_o = 45^\circ$. Thus the PPPAR has a higher azimuth resolution everywhere else in the domain of interest but a slightly lower elevation resolution for beam elevations less than about 20°.

Electrically scanning arrays are presented with the problem where there are changes in the H and V gains as the beam scans [30]. These gain changes contribute to biases in reflectivity factor Z, as well as differential reflectivity Z_{DR}, because gain changes are not necessarily equal and depend on the beam direction. These contributions to bias in polarimetric parameter estimates can be partially eliminated by adjusting the excitation of the H and/or V ports to equalize the received copolar H and V voltages for each beam direction.

CPPAR Element Weighting: The weights w_{mn} applied to the elements of the CPPAR are [31]

$$w_{mn} = \left(\frac{\left\{1-4\left[R^2\sin^2(\phi_o-\phi_n)+z_m^2\right]/D^2\right\}^a + b}{1+b}\right) \tag{3}$$

where $R = 6$ m is the radius of the cylinder, z_m is the vertical distance of the mth row from the center of the cylinder, $D = 8.54$ m is the axial length of the cylindrical array, and the CPPAR beam is pointed in the (θ_o, ϕ_o) direction. ϕ_n is the azimuth angle of the nth column relative to the azimuth ϕ_0 of the beam [see Fig. 2(c)]. As with the PPPAR, to approximately match the aperture distribution of the WSR-88D, $a = 3$, and $b = 0.16$. As we shall see, the radiation patterns of the CPPAR are reasonably matched to those of the WSR-88D.

C. Radiation Patterns of the Patch Array Element

The antenna element considered in this paper—the same for both the PPPAR and CPPAR—is a single-layered $0.32\lambda_o$ square probe-fed patch on a substrate with a permittivity of 2.2 and a thickness of 0.0142 λ_o with a ground plane size of $0.81\lambda_o$ [see Fig. 3(a)]. The substrate size is as large as the ground plane. The probe feed location is 0.045 λ_o to the center of the patch, and the probe feed has an inside center conductor with a radius of 0.0039 λ_o and an outer conductor with a radius of 0.0090 λ_o. The element separation is $0.5\lambda_o$ for both the PPPAR and CPPAR, and the mutual coupling between elements is neglected. Fulton [11] showed that the patterns of a patch element in a large array are similar to that of a single patch even though there is mutual coupling. Although the radiation patterns of a patch on a finite ground plane differ from those patterns of a patch on a conducting cylindrical or planar surface and although mutual coupling will alter the radiation pattern of the patch embedded in the array, the methodology presented herein can use the radiation pattern of patches mounted on realistic structures.

The high frequency structural simulator (HFSS; available online at http://www.ansys.com/Products/Simulation+Technology/Electromagnetics/Signal+Integrity/ANSYS+HFSS)), a commercial finite-element method solver for electromagnetic structures from ANSYS, is used to compute the copolar and

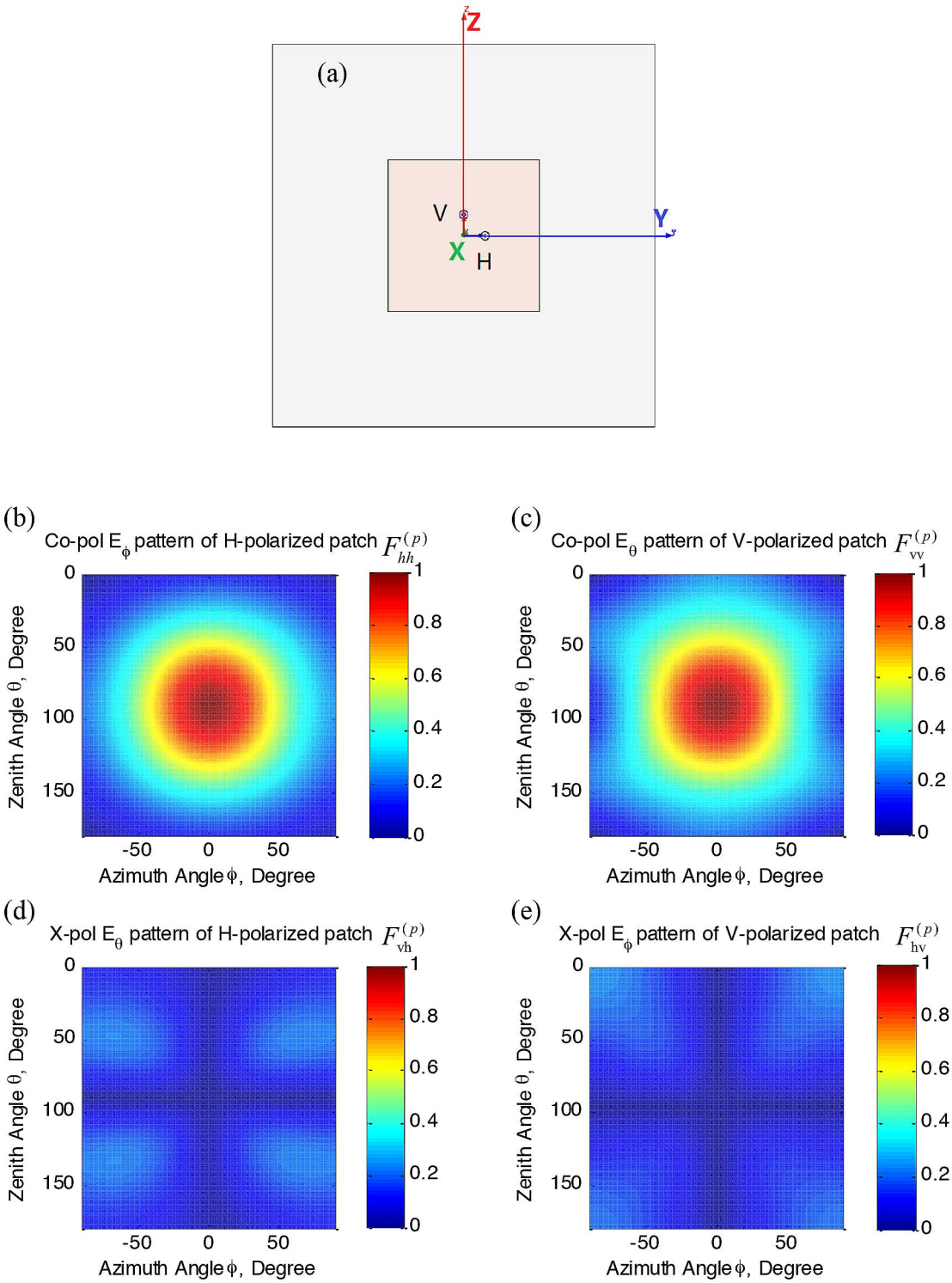

Fig. 3. HFSS-simulated patch element radiation patterns normalized by the copolar peak (equal for H and V polarizations).

cross-polar radiation fields of the patch. The H and V copolar and cross-polar patterns of the array are obtained by coherently adding the fields from each element of the array for both the CPPAR and PPPAR—an array factor could have been used for the PPPAR but not for the CPPAR [14, ch. 2]; thus, realistic main lobe and sidelobes are considered.

These theoretically deduced realistic radiation patterns for the array are used to calculate the biases of Z_{DR} and ρ_{hv} presented in Section III. It should be noted that the probe-fed excitation of the patch antenna generates higher order standing wave modes, although of lesser intensity than the fundamental TM_{010} and TM_{001} modes in the open-ended patch cavity (e.g., TM_{010} generates copolar H fields; TM_{001} generates copolar V fields). Higher order modes cause slightly asymmetrical radiation patterns as seen in Fig. 3 (e.g., the horizontal null line in Fig. 3(e) is at about $\theta = 96°$, not the 90° that it

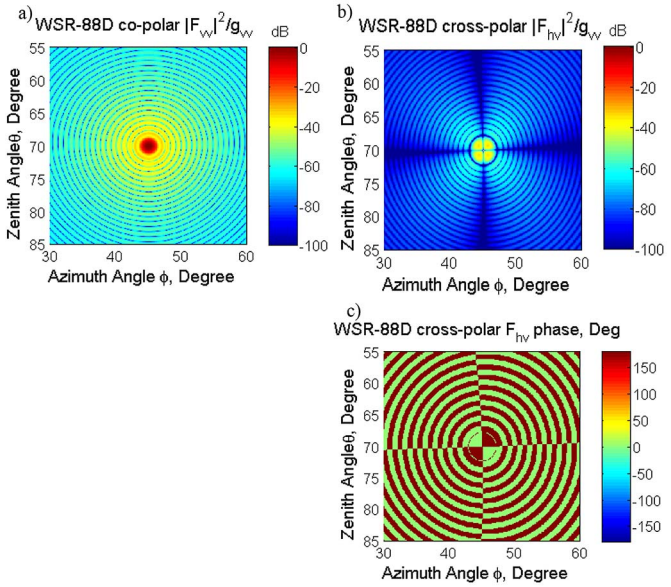

Fig. 4. Normalized theoretical one-way radiation patterns of KOUN for (a) the copolar E_θ, (b) the cross-polar E_ϕ, and (c) the cross-polar phase. Wavelength $\lambda = 11.09$ cm. The beam is directed at $\theta_o = 70^\circ$ and $\phi_o = 45^\circ$.

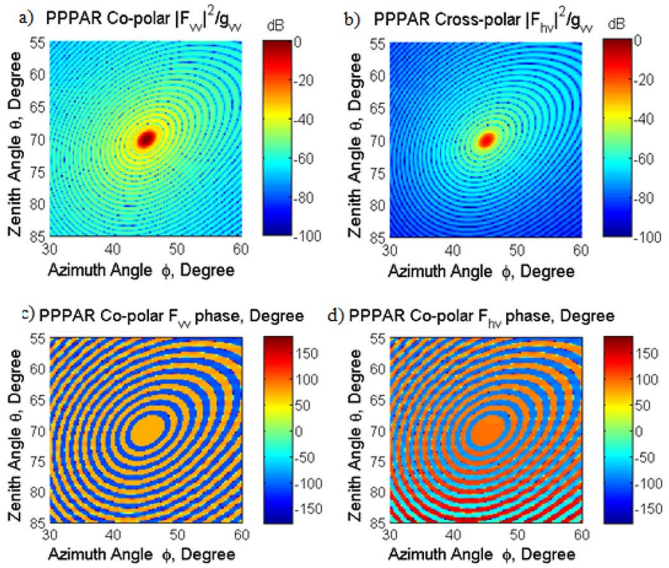

Fig. 5. One-way power density patterns of a PPPAR array normalized by the $F_{\rm vv}$ gain at (45°, 90°). (a) Copolar E_θ field, (b) the cross-polar E_φ field, (c) the copolar phase, and (d) the cross-polar phase. The beam is directed at $\theta_o = 70^\circ$ and $\phi_o = 45^\circ$.

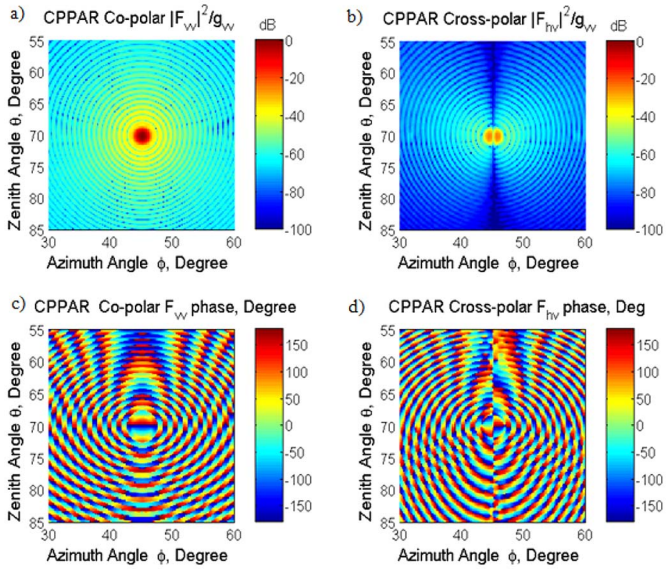

Fig. 6. One-way power density patterns of the CPPAR array, normalized by gain $g_{\rm vv}$. (a) Copolar E_θ field, (b) the cross-polar E_φ field, (c) the copolar phase, and (d) the cross-polar phase. The beam is directed at $\theta_o = 70^\circ$ and $\phi_o = 45^\circ$.

would have if only the fundamental mode was present; this can result in the array null slight shifted a little angle due to the asymmetric of the element pattern). This asymmetrical radiation patterns can also be found in [3]. However, because the H port probe is symmetrical about the horizontal line, the cross-polar null in Fig. 3(d) is at $\theta = 90^\circ$. Mirror arrangement of the patches can eliminate asymmetry, which should result in a lower cross-polar field along the horizontal plane as seen in experiments [21].

Fig. 3(b)–(e) presents the patch's radiation field. $F_{\rm vv}^{(p)}$ is the copolar pattern of the V field (E_θ) if the V port is energized and vice versa for $F_{\rm hh}^{(p)}$. $F_{\rm hv}^{(p)}$ is the cross-polar H (E_ϕ) pattern if the V port is energized and vice versa for $F_{\rm vh}^{(p)}$. Both copolar and cross-polar patterns are normalized by the peak of $F_{\rm vv}^{(p)}$. Because the polarization definition shown here is definition 2 in [17, Fig. 1], the pattern of the vertically polarized aperture is not simply the pattern of the horizontally polarized aperture rotated 90° in the y-z plane as seen by comparing copolar and cross-polar patterns in Fig. 3.

Comparing patch patterns of the full-wave simulated one (see Fig. 3) with that of the one defined in [15] in which the field due to so-called nonradiating slots ([1], chapter 14) has been ignored, it is seen that cross-polar fields are due to both radiating and "non-radiating" slots; the radiating slots cause the geometrically induced cross-polar field. Although it is not shown here, the patch patterns considering both the radiating slots and nonradiating slots agree very well with the HFSS-simulated patch patterns. It should also be noted that the copolar phases of realistic patterns are not necessarily equal and zero as assumed in [35] and the phases can be a function of θ, φ, etc., as is seen in the phase plots not shown here. Thus, in our computation of biases, the amplitude and phases of the copolar and cross-polar patterns, which are dependent on the beam direction, are included.

D. Theoretical Radiation Patterns of the Three Polarimetric Radars

Patterns of radiation from the WSR-88D, PPPAR, and CPPAR are shown in Figs. 4–7, respectively. All patterns at broadside have type-2 cross-polar fields as defined in [35]—a quad of four cross-polar peaks of alternating phase symmetrically located about the copolar beam. Only the PPPAR radiation pattern evolves into the type-1 cross-polar pattern (i.e., cross-polar radiation main lobe coaxial with the copolar beam) as the beam is steered away from the principal planes—it is the type-1 pattern that is the most effective in creating the polarimetric parameter estimate bias.

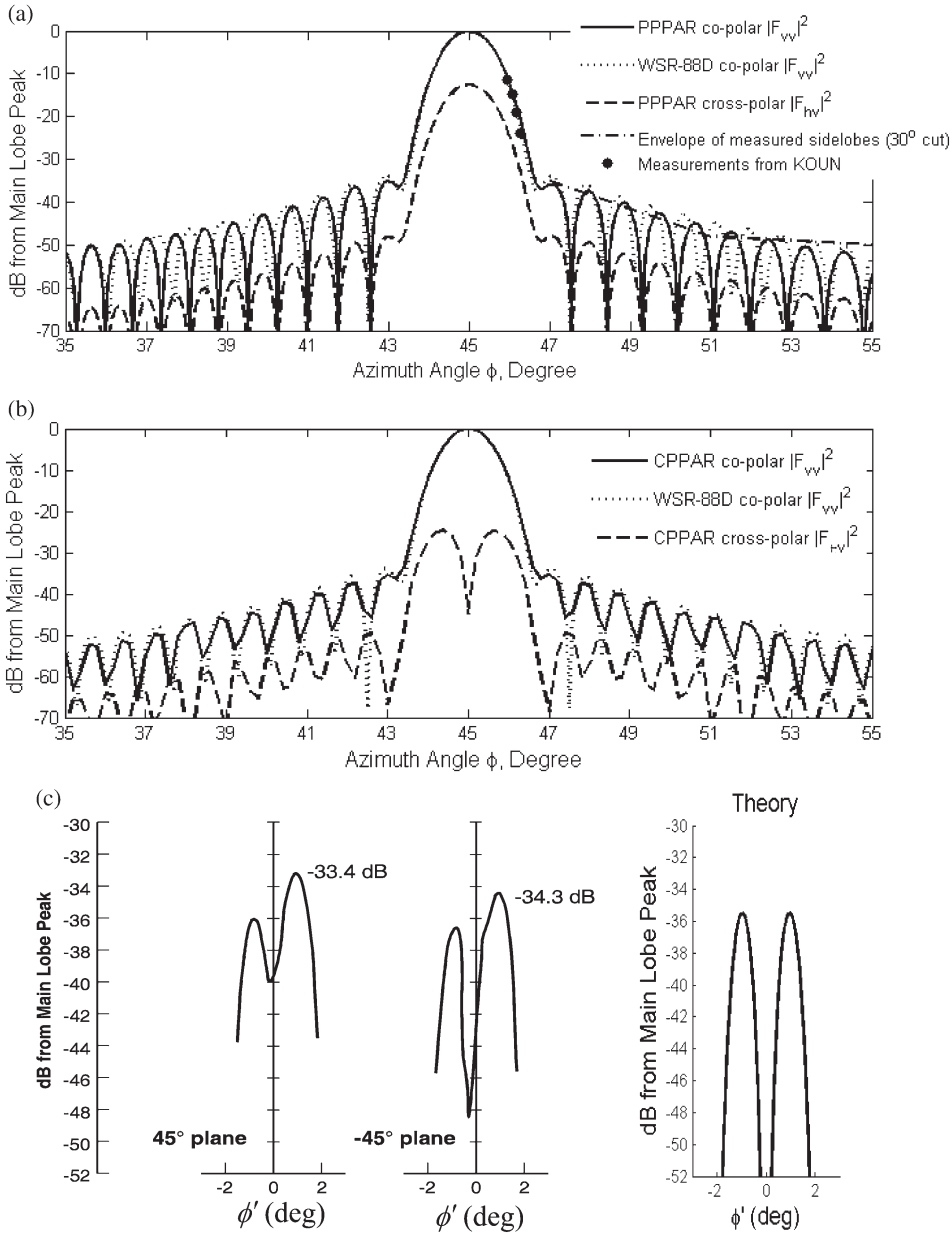

Fig. 7. Comparison of the theoretical and measured copolar $|F_{\rm vv}|^2$ and cross-polar $|F_{\rm hv}|^2$ radiation patterns of (a) PPPAR and WSR-88D and (b) CPPAR and WSR-88D. The beam is directed at $\theta_o = 70^\circ$ and $\phi_o = 45^\circ$, for frequency = 2905 MHz. (c) Theoretical and measured $|F_{\rm hv}|^2$ as a function of θ' for the WSR-88D along a $\phi' = \pm 45^\circ$ cut.

For these four figures, the beam pointing elevation angle θ_e ($\theta_e = 90^\circ - \theta_0$) for all three antennas is chosen to be at 20° which is typically the highest elevation angle for weather radar, and the azimuth for all three beams is $\phi_o = 45^\circ$. This extreme limit of the scanned sector gives the condition for maximum bias and gain change. All patterns of radiation are presented using the coordinate system of Fig. 1. Fvv, etc., are elements of the electric field radiation matrix $\overleftrightarrow{\mathbf{F}}$ defined by Zrnić *et al.* [35]. For the phased array, $\overleftrightarrow{\mathbf{F}}$ includes both the element factor and array factor, and $\overleftrightarrow{\mathbf{F}}$ is the coherent addition of all the array elements. $F_{\rm vv}$ is the copolar pattern of E_θ if the V port is energized and vice versa for $F_{\rm hh}$. $F_{\rm hv}$ is proportional to the cross-polar H field (E_ϕ) if the V port of the array is energized and vice versa for $F_{\rm vh}$. Both copolar and cross-pol patterns in this paper are normalized by $F_{\rm vv}$ along the beam axis. Moreover, $F_{\rm ij} = \sqrt{g_{\rm ij}} f_{\rm ij}(\theta, \phi; \theta_0, \phi_0)$ where $f_{\rm ij}(\theta, \phi; \theta_0, \phi_0) = |f_{\rm ij}(\theta, \phi; \theta_0, \phi_0)| \exp[j\gamma_{ij}(\theta, \phi; \theta_0, \phi_0)]$)—in the coordinated system of Fig. 1, radiation patterns are functions of the beam direction.

WSR-88D Radiation Patterns: The copolar and cross-polar radiation amplitude patterns are calculated using theoretical formulations (see Appendix A) and then compared with measurements—$F_{\rm hh}$ and $F_{\rm vv}$ patterns are identical as are $F_{\rm hv}$ and $F_{\rm vh}$. Because the theoretical and measured patterns are given in the (r, θ', ϕ') spherical coordinate system in which the polar axis is along the beam axis, Appendix B gives the transformation to plot the WSR-88D radiation patterns in the

(r, θ, ϕ) spherical coordinate system (see Fig. 1) used by radar meteorologists, so meaningful comparisons can be made.

The theoretical patterns of WSR-88D pointing at $(\theta_o, \phi_o) = (70^\circ, 45^\circ)$ are shown in Fig. 4. Although not apparent in these figures, the WSR-88D patterns are slightly distorted (i.e., not circularly symmetric in the (θ, ϕ) displays) due to the coordinate system transformation (see Appendix B)—the lack of circular symmetry is, however, evident in the sidelobe patterns. Four equal cross-polar main lobes have an alternating phase [see Fig. 4(c)], and the copolar phase is a constant through all the angles.

The PPPAR Radiation Patterns: The copolar and cross-polar fields are shown in Fig. 5(a) and b for the case in which copolar V (i.e., E_θ) is principally radiated. The cross-polar E_ϕ field pattern of the PPPAR has a main lobe coaxial with the copolar beam and has a peak 12.4 dB below the copolar peak at the main beam direction. Although not shown here, the cross-polar peak is -11.2 dB below the copolar peak of the horizontal polarization. As will be shown in Section III, this geometrically induced cross-polar field and the difference of H and V gains cause a significant bias. The copolar and cross-polar fields are the fields of the element pattern multiplied by the array factor. Thus, the cross-polarization nulls of the element patterns remain along the principal planes which are slightly shifted a few degrees from the $(\theta, \phi = 0^\circ)$ and $(\theta = 90^\circ, \phi)$ of an ideal patch as discussed earlier.

Both the copolar and cross-polar beams have elliptical cross sections determined by the array factor. The orientation of the elliptically shaped beam and the major to minor axis ratio is a function of the beam direction—not so for the invariant circular beam of the WSR-88D. The PPPAR beam is only circular at $(\theta_o = 90^\circ, \phi_o = 45^\circ)$ with a beamwidth equal to that of the WSR-88D—Fig. 7(a) shows relatively good agreement of the main lobe, even when $\theta_o = 70^\circ$, $\phi_o = 45^\circ$, but sidelobe locations differ. Although not shown, the broadside PPPAR beam has a higher gain and a better azimuth resolution than the WSR-88D. This is because, at broadside, the aperture of the PPPAR is azimuthally larger than that of the WSR-88D (see Fig. 2). At $(\theta_o, \phi_o) = (90^\circ, 45^\circ)$, the PPPAR gain is the same as that of WSR-88D, but at $(\theta_o, \phi_o) = (70^\circ, 45^\circ)$, it is 0.2 dB less than that of WSR-88D due to the slightly less effective aperture. In Fig. 5(c) and (d), the phase at the boresight of the copolar field is 72°, and the phase at the boresight of the cross-polar field is 91°. This illustrates that the gain, as well as the phases, is a function of beam direction—thus, corrections to eliminate bias will be a function of beam direction.

The CPPAR Radiation Patterns: Fig. 6 shows the copolar and cross-polar radiation patterns for the CPPAR. The CPPAR gain at $(\theta_o, \phi_o) = (70^\circ, 45^\circ)$ is 0.2 dB less than that of the WSR-88D due to the less effective area. The copolar beams of the CPPAR and WSR-88D are reasonably matched at the extreme elevation angle of 20° [see Fig. 7(b)]. Although not shown, the cross-polar field pattern of CPPAR with the beam directed at 96.2° zenith (90° zenith angle for an ideal patch) has a quadrant of equal amplitude main lobes (about -36 dB) equally spaced around the copolar beam, as does the WSR-88D which also has cross-polar peaks at about -36 dB [see Fig. 7(c)]. However, unlike the WSR-88D for which the quad of four main lobes does not change as the elevation angle changes, the intensity of the pair of cross-polar peaks below the zenith angle 96.2° plane (or below the horizontal principal plane for an ideal patch) decreases in intensity, but the pair above, of equal amplitude and spaced about a half a beamwidth from the vertical principal plane, follows the copolar beam and increases in intensity with the increase of the elevation angle. The quadrant peaks shift from being centered about a zenith angle of 90° for an ideal patch to 96.2° for a simulated patch (see Fig. 3); as stated earlier, this is due to the unsymmetrical pattern [see Fig. 3(e)] of the simulated patch caused by higher order modes in the patch cavity.

The vertical principal plane always bisects the cross-polar beam and forms a pair of cross-polar main lobes of opposite phase and equal peak magnitudes of -24.9 dB at $\theta_o = 70^\circ$. Whereas the PPPAR has a -12.4 dB boresight peak, the CPPAR cross-polar field is zero. The pair of cross-polar main lobes [see Fig. 6(b)] are displaced from the boresight by about 0.6° [see Fig. 7(b)], and each has a 3-dB beamwidth of about 0.6°. In the vertical direction, the cross-polar main lobes have a 3-dB beamwidth of about 1°.

Because the CPPAR and WSR-88D have nearly the same aperture distribution, the copolar radiation patterns at broadside (i.e., $\theta_o = 90^\circ$, but any ϕ_o) are nearly in agreement about the main lobe of the copolar beam—comparisons of these patterns [see Fig. 7(b)] show this to be true.

E. Comparison of Theoretical Radiation Patterns With Measured and Simulated Ones

The line plots in Fig. 7(a)–(c) compare the copolar and cross-polar radiation patterns of PPPAR, CPPAR, and the WSR-88D at the limit of the scan region (i.e., azimuth of 45°) where the PPPAR geometrically induced cross-polar fields are the maximum.

In Fig. 7(a), the PPPAR copolar pattern is very similar to that of WSR-88D near the main lobe. The PPPAR pattern is not symmetric about $\phi_o = 45^\circ$ in azimuth (as can also be seen from Fig. 5), and the sidelobes for PPPAR are slightly higher and the sidelobe widths are slightly narrower at $\phi < 45^\circ$ than $\phi > 45^\circ$. These differences are due to the changes in the projection of the PPPAR's array area (e.g., larger for $\phi < 45^\circ$ than for $\phi > 45^\circ$).

The sidelobes of the WSR-88D were measured by Andrew Canada along the 30° cut [19], and an eyeball estimate of the envelope of these sidelobes at $\theta' > 2^\circ$ is shown with a dash-dotted line [8]. This pattern cut lies midway between the narrow ridges of higher sidelobes (about 5 to 13 dB higher) due to the blockages by the spars and is therefore more representative of the sidelobe levels of the WSR-88D. The KOUN main lobe measurements (dots) are also obtained from [8].

The transformation in Appendix B) is applied to the theoretical and measured data, and thus, the beamwidth, in the (θ, ϕ) coordinates of Fig. 1, is slightly larger after the transformation. Specifically, for measurement data in Fig. 7, the azimuth beamwidth changed from 0.9° at $(\theta_o, \phi_o) = (90^\circ, 0^\circ)$ to 0.96° at $(\theta_o, \phi_o) = (70^\circ, 45^\circ)$. Although the beamwidth of the WSR-88D measured in the spherical coordinate system with the polar

axis along the beam does not change with the elevation angle, it does change when measured in the coordinate system of Fig. 1.

The CPPAR copolar pattern is very similar to that of WSR-88D near the main lobe [see Fig. 7(b)]. Slight differences arise because, for the beam at $(\theta_o, \phi_o) = (70^\circ, 45^\circ)$, the CPPAR beam deviates slightly from the circular shape seen at broadside. WSR-88D sidelobe levels beyond 10° azimuth are more than 50 dB below the copolar peak and are in agreement with measurements. The theoretical and measured sidelobe levels also agree well with the sidelobe levels measured for a dual-offset fed antenna having ultralow sidelobes needed for weather radar research [5]. At the elevation angles of 0°, 20°, and 30°, the pair of CPPAR cross-polar peaks are -37 dB, -25 dB, and -22 dB below the copolar peak. The cross-polar peaks of the dual-offset fed reflector are also two (versus the four for a center-fed parabolic antenna), and each has a peak gain at about -35.5 dB below the copolar gain [5] similar to that for the CPPAR if the copolar beam is pointed at $\theta_0 = 90^\circ$.

The measured cross-polar $F_{\rm hv}$ field of WSR-88D can be found in [35, Fig. 7], but it is reproduced in Fig. 7(c) to compare with the theoretical pattern computed in Appendix A and shown in Fig. 4(b). The line plot in Fig. 7(c) is along $\phi' = 45^\circ$ and is plotted as a function of θ' (θ' and ϕ' are defined in Appendix A).

In summary, we showed the radiation patterns of the WSR-88D, PPPAR, and CPPAR and made comparisons of pattern characteristics. By using the similar aperture size and weighting, the normalized copolar patterns of phased arrays are almost the same as that of WSR-88D. However, the cross-polar pattern peak of PPPAR is high and coincident with the copolar peak, whereas the CPPAR has a cross-polar null at the copolar peak. A cross-polar peak coincident with the copolar peak causes much larger polarimetric parameter biases than if the cross-polar peak is displaced from the copolar peak as is shown in Section III.

III. Comparing Theoretical Biases in Estimates of Polarimetric Variables using CPPAR, PPPAR, and the WSR-88D

Galletti and Zrnić [12] and Zrnić *et al.* [35] calculated theoretical biases of $Z_{\rm DR}$ and $\rho_{\rm hv}$ estimates for a center-fed parabolic reflector antenna when either the SHV or the AHV modes of polarimetric data collection are used. Zrnić *et al.* [35] introduce the SHV notation that defines copolar H and V waves of equal amplitude transmitted along the beam axis. Here, we apply the notation STSR to designate that the H and V ports of the array antenna are simultaneously excited with equal voltages (for the parabolic antenna, SHV and AHV are synonymous with STSR and ATSR).

A Gaussian function was used by Zrnić *et al.* [35] to model the copolar and cross-polar main lobes for the radiation patterns of parabolic reflector antennas. Although the main lobe is reasonably modeled by the Gaussian function, sidelobes are not. Furthermore, unlike the assumptions made by Zrnić *et al.* [35], the copolar radiation pattern functions $F_{\rm hh}$ and $F_{\rm vv}$ for PPARS are not necessarily equal and real Gaussian functions but are complex variables that are functions of θ, φ. Moreover, for the reflector antenna, we use realistic radiation patterns to calculate the biases of $Z_{\rm DR}$ and $\rho_{\rm hv}$. Nevertheless, the approach of Zrnić *et al.* [35] can be generalized to compute biases for PPARs and parabolic reflector antennas having realistic radiation patterns. For the mechanically steered parabolic reflector, there are no variations with direction, but for PPARs, the biases are functions of the beam scanning angle.

The HFSS-computed element pattern is used to obtain the array's copolar and cross-polar radiation patterns having phase and amplitude that vary across the beam and are functions of beam direction. General formulas for the biases are derived in terms of radiation matrix elements given any kind of array element, but results are presented for patch elements on planar and cylindrical surfaces, and operating at a frequency of 2.705 GHz (this frequency has been chosen because it is the one for KOUN), a prototype dual-polarimetric WSR-88D for which we have radiation pattern measurements to compare with theoretical patterns is presented in Section II.

A. STSR Mode

To simplify calculations without sacrificing the objectives of this paper, $Z_{\rm DR}$, $\rho_{\rm hv}$, and $\phi_{\rm dp}$ biases are calculated under the following conditions: 1) The intrinsic $Z_{\rm DR}$ is produced by oblate hydrometeors having zero canting angles projected onto a plane perpendicular to the beam axis; thus, the off-diagonal terms of the backscattering matrix $\overleftrightarrow{\mathbf{S}}$ are zero; 2) differential attenuation due to precipitation along the path of propagation can be neglected at 10-cm wavelengths, but differential phase shift $\Phi_{\rm dp}$ cannot [35]; and 3) reflectivity is spatially uniform. To simplify notation, the phase shifts $\phi_{\rm hh}$, and $\phi_{\rm vv}$ incurred during H and V propagation are incorporated into the backscattering matrix $\overleftrightarrow{\mathbf{S}}$ (e.g., $\phi_{\rm hh}$ is combined with $\delta_{\rm hh}$, the phase shift upon backscatter for the H wave).

For the STSR mode, the matrix equation for the incremental voltages received in the H and V channels due to backscatter from a hydrometeor is given by [35]

$$\begin{bmatrix} \delta V_{\rm rh} \\ \delta V_{\rm rv} \end{bmatrix} \equiv \mathbf{V}_{\rm r} = \overleftrightarrow{\mathbf{F}}^{\mathbf{T}} \overleftrightarrow{\mathbf{S}} \overleftrightarrow{\mathbf{F}} \vec{\mathbf{V}}_{\mathbf{t}} = \begin{bmatrix} F_{\rm hh} & F_{\rm vh} \\ F_{\rm hv} & F_{\rm vv} \end{bmatrix} \begin{bmatrix} S'_{\rm hh} & 0 \\ 0 & s_{\rm vv} \end{bmatrix} \begin{bmatrix} F_{\rm hh} & F_{\rm hv} \\ F_{\rm vh} & F_{\rm vv} \end{bmatrix} \begin{bmatrix} V_{\rm th} \\ V_{\rm tv} \end{bmatrix} \quad (4)$$

where $\overleftrightarrow{\mathbf{S}}$ is the backscattering matrix. To account for differential propagation phase shift $\phi_{\rm dp}$ to and from the scatter, $s'_{\rm hh} = s_{\rm hh} e^{j\phi_{\rm dp}}$. $V_{\rm th}$ and $V_{\rm tv}$ are voltages applied simultaneously to the H and V antenna ports (for the array, it is assumed that all element H and V voltages with weights specified by (2) and (3) are connected to a single H and V antenna port).

Zrnić *et al.* [35] considered a phase difference β between the applied H and V voltages and assumed transmission lines from the antenna port to the element to be of equal length. The worst case $Z_{\rm DR}$ bias has been shown to occur for coaxial copolar and cross-polar beams if $\beta = 90^\circ$ and if the phase difference between the copolar and cross-polar fields is in phase quadrature at the antenna. Moreover, the propagation effect is ignored. In this case, the coaxial cross-polar peak needs to be 50 dB or more below the co-polar peak to ensure that the $Z_{\rm DR}$ bias is less than 0.1 dB. β can be controlled, and if $\beta = 0^\circ$or

180° (i.e., transmitted polarization is linear at a slant of 45° or 135°), the acceptable cross-polar peak can be decreased to 45 dB below the copolar peak, a relatively small 5-dB improvement. To simplify and to focus on the more significant bias sources associated with PPARs, we assume $\beta = 0°$ and $V_{\rm th} = V_{\rm tv} = 1$. Constants of proportionality are to make (4) dimensionally correct, and the arguments of $F_{\rm ij}$ and $s_{\rm ij}$ are omitted to shorten the notation.

Equation (4) is applied to a single hydrometeor, but what is of interest is a spatial distribution of scatterers weighted by radiation pattern matrix elements. Under the condition that the echoes from the neighboring areas are uncorrelated, the expected powers received in the H and V channels are [35]

$$P_{\rm h} \sim \int_{\Omega} \left\langle |\delta V_{\rm rh}|^2 \right\rangle d\Omega \tag{5}$$

$$P_{\rm v} \sim \int_{\Omega} \left\langle |\delta V_{\rm rv}|^2 \right\rangle d\Omega. \tag{6}$$

The bias of $Z_{\rm DR}$ in decibels is computed by subtracting the true value of $Z_{\rm DR}$ from the estimated one. Thus, bias($Z_{\rm DR}$) is given by

$$\text{bias}(Z_{\rm DR} = 10\cdot\log(P_{\rm h}/P_{\rm v} - Z_{\rm DR}^{\rm true} = 10\cdot\log(B_1/B_2) - Z_{\rm DR}^{\rm true} \tag{7}$$

where

$$\begin{aligned} B_1 &= \frac{\int_{\Omega} \left\langle |\delta V_{\rm rh}|^2 \right\rangle d\Omega}{\left\langle |s_{\rm vv}|^2 \right\rangle} \\ &= Z_{\rm dr} \int_{\Omega} \Big\{ |F_{\rm hh}|^4 + |F_{\rm hh}|^2 |F_{\rm hv}|^2 + 2|F_{\rm hh}|^2 {\rm Re}(F_{\rm hh}^* F_{\rm hv}) + Z_{\rm dr}^{-1} \\ &\quad \times \Big[|F_{\rm vh}|^2 |F_{\rm vv}|^2 + |F_{\rm vh}|^4 + 2\,|F_{\rm vh}|^2 {\rm Re}(F_{\rm vh}^* F_{\rm vv}) \Big] + 2 \\ &\quad \times |\rho_{\rm hv}(0)|\, Z_{\rm dr}^{-0.5} {\rm Re}\big[e^{-j\phi_{\rm dp}} \big(F_{\rm hh}^{*2} F_{\rm vh}^2 + F_{\rm hh}^* F_{\rm hv}^* F_{\rm vh}^2 \\ &\qquad + F_{\rm hh}^{*2} F_{\rm vh} F_{\rm vv} + F_{\rm hh}^* \\ &\qquad \times F_{\rm hv}^* F_{\rm vv} F_{\rm vh} \big) \big] \Big\}\, d\Omega \end{aligned} \tag{8}$$

$$\begin{aligned} B_2 &= \frac{\int_{\Omega} \left\langle |\delta V_{\rm rv}|^2 \right\rangle d\Omega}{\left\langle |s_{\rm vv}|^2 \right\rangle} \\ &= \int_{\Omega} \Big\{ |F_{\rm vv}|^4 + |F_{\rm vv}|^2\, |F_{\rm vh}|^2 + 2\,|F_{\rm vv}|^2\, {\rm Re}(F_{\rm vv}^* F_{\rm vh}) + Z_{\rm dr} \\ &\quad \times \Big[|F_{\rm hh}|^2 |F_{\rm hv}|^2 + |F_{\rm hv}|^4 + 2\,|F_{\rm hv}|^2 {\rm Re}(F_{\rm hv}^* F_{\rm hh}) \Big] + 2 \\ &\quad \times |\rho_{\rm hv}(0)| Z_{\rm dr}^{0.5} {\rm Re}\,\big[e^{-j\phi_{\rm dp}} \big(F_{\rm hv}^{*2} F_{\rm vv}^2 + F_{\rm hv}^* F_{\rm hh}^* F_{\rm vv}^2 \\ &\qquad + F_{\rm hv}^{*2} F_{\rm vv} F_{\rm vh} + F_{\rm hh}^* \\ &\qquad \times F_{\rm hv}^* F_{\rm vv} F_{\rm vh} \big) \big] \Big\}\, d\Omega. \end{aligned} \tag{9}$$

Equations (8) and (9) are obtained by substituting (4) into (5) and (6). Lower case "dr" on Z indicates the ratio of H and V received powers, whereas the upper case "DR" subscript denotes $Z_{\rm DR}$ in logarithmic units.

The biases of copolar correlation coefficient magnitude $|\rho_{\rm hv}|$ and differential phase $\phi_{\rm dp}$ are given by

$$\text{bias}(|\rho_{\rm hv}|) = \frac{|\langle \delta V_{\rm rh}^* \delta V_{\rm rv} \rangle|}{\sqrt{\left\langle |\delta V_{\rm rh}|^2 \right\rangle \left\langle |\delta V_{\rm rv}|^2 \right\rangle}} - \left|\rho_{\rm hv}^{\rm true}\right| \tag{10a}$$

$$\text{bias}(\phi_{\rm dp}) = \text{angle}\left(\frac{\langle \delta V_{\rm rh}^* \delta V_{\rm rv} \rangle}{\sqrt{\left\langle |\delta V_{\rm rh}|^2 \right\rangle \left\langle |\delta V_{\rm rv}|^2 \right\rangle}} \right) - \phi_{\rm dp}^{\rm true}. \tag{10b}$$

The biases of $|\rho_{\rm hv}|$ and differential phase $\phi_{\rm dp}$ can be rewritten as

$$\text{bias}(|\rho_{\rm hv}|) = \frac{|B_3|}{\sqrt{B_1 B_2}} - \left|\rho_{\rm hv}^{\rm true}\right| \tag{11a}$$

$$\text{bias}(\phi_{\rm dp}) = \text{angle}\left(\frac{B_3}{\sqrt{B_1 B_2}} \right) - \phi_{\rm dp}^{\rm true} \tag{11b}$$

where B_3 is

$$\begin{aligned} B_3 &= \frac{\int_{\Omega} \langle \delta V_{\rm rh}^* \delta V_{\rm rv} \rangle\, d\Omega}{\left\langle |s_{\rm vv}|^2 \right\rangle} \\ &= \int_{\Omega} \Big[Z_{\rm dr} \Big(|F_{\rm hh}|^2\, F_{\rm hh}^* F_{\rm hv} + F_{\rm hh}^{*2} F_{\rm hv}^2 + |F_{\rm hh}|^2 |F_{\rm hv}|^2 \\ &\qquad + F_{\rm hh}^* F_{\rm hv} |F_{\rm hv}|^2 \Big) + |F_{\rm vv}|^2 F_{\rm vv} F_{\rm vh}^* + F_{\rm vv}^2 F_{\rm vh}^{*2} \\ &\quad + |F_{\rm vv}|^2\, |F_{\rm vh}|^2 + |\rho_{\rm hv}(0)| e^{-j\phi_{\rm dp}} Z_{\rm dr}^{0.5} \\ &\quad \times \left(F_{\rm hh}^{*2} F_{\rm vv}^2 + F_{\rm hh}^{*2} F_{\rm vv} F_{\rm vh} + F_{\rm hh}^* F_{\rm vv}^2 F_{\rm hv}^* \right) \\ &\quad + |\rho_{\rm hv}(0)| e^{j\phi_{\rm dp}} Z_{\rm dr}^{0.5} \left(F_{\rm vh}^{*2} F_{\rm hv}^2 + F_{\rm vh}^{*2} F_{\rm hv} F_{\rm hh} \right. \\ &\qquad \left. + F_{\rm vh}^* F_{\rm vv}^* F_{\rm hv}^2 \right) \\ &\quad + 2|\rho_{\rm hv}(0)| Z_{\rm dr}^{0.5} {\rm Re}\left(e^{-j\phi_{\rm dp}} F_{\rm hh}^* F_{\rm hv}^* F_{\rm vv} F_{\rm vh} \right) \Big]\, d\Omega. \end{aligned} \tag{12}$$

Fig. 8 shows the biases of $Z_{\rm DR}$, $|\rho_{\rm hv}|$, and $\phi_{\rm dp}$ as functions of θ_e with $\phi_0 = 45°$ for the three antennas operating in the STSR mode. Here, we assume that true $Z_{\rm DR}$ is a constant independent of elevation angle. There are multiple sources of cross-polar fields that can cause bias (e.g., radiation from the so-called nonradiating sides of the patch in [1, ch. 14]; edge effects associated with the finite-size ground plane; geometrically induced cross-polar field, etc.). Another source of bias is the differential gains in the H and V copolar radiation patterns of the patch.

In Fig. 8, the PPPAR and CPPAR elements have weights given by (2) and (3) but without density and element orientation compensation. Both the bias caused by the geometrically induced cross-polar field and the bias caused by differential gains in the element's H and V fields contribute to the biases shown (see Fig. 8). In Fig. 8(a), as the elevation angle increases, the PPPAR $Z_{\rm DR}$ bias decreases because the horizontally polarized patch fields [see Fig. 3(b)] reduce more than the vertical polarized patch fields [see Fig. 3(c)].

CPPAR has much lower $Z_{\rm DR}$ and $\rho_{\rm hv}$ biases than the PPPAR. Because the CPPAR beam is azimuthally steered by commutation, the beam is always in a vertical principal plane which

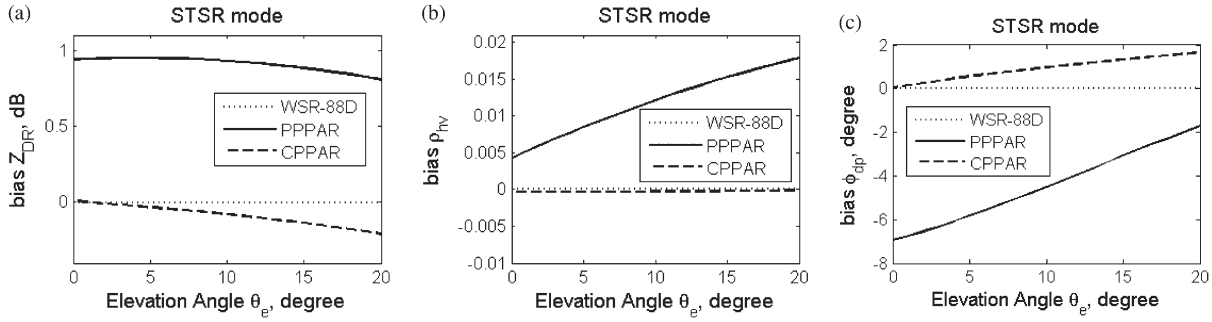

Fig. 8. Biases versus the beam's elevation angle θ_e for the STSR mode. $\rho_{\rm hv} = 0.90$, $Z_{dr} = 1$, and $\phi_{\rm dp} = 0$. The beam is pointed at $\phi_0 = 45°$, (a) $Z_{\rm DR}$ bias, (b) $\rho_{\rm hv}$ bias, and (c) $\phi_{\rm dp}$ bias.

rotates azimuthally and synchronously with the beam. If the H and V gains of the patch were matched, the theoretically bias of the CPPAR would be zero as is the bias for the WSR-88D. Therefore, the small negative increase of the $Z_{\rm DR}$ bias for the CPPAR [see Fig. 8(a)] is due to the differential gain of the patch.

Applying (7)–(12) to the theoretical patterns of WSR-88D and integrating θ and ϕ from $-30°$ to $30°$, the $Z_{\rm DR}$ and $\rho_{\rm hv}$ biases for WSR-88D are obtained. To save computational time, we choose $\pm$ 30° about the boresight—because most powers located inside this region and integration outside this region do not affect the results. The $Z_{\rm DR}$ bias is -0.0005 dB. In [35], the $Z_{\rm DR}$ bias, assuming a Gaussian shape for the main lobe for the cross-polar field and having a peak of -35.5 dB, is about -0.0016 dB.

B. ATSR Mode

For the ATSR mode, we alternately set $V_{\rm th}$ to 1 and 0 and vice versa for $V_{\rm tv}$. The copolar H and cross-polar echo voltages deduced from (6) are

$$\delta V_{\rm rh} = F_{\rm hh}^2 s_{\rm hh} + F_{\rm vh}^2 s_{\rm vv}, \quad \text{copolar} \tag{13}$$

$$\delta V_{\rm rv} = F_{\rm hh} F_{\rm hv} s_{\rm hh} + F_{\rm vv} F_{\rm vh} s_{\rm vv} \quad \text{cross-polar} \tag{14}$$

if $V_{\rm th} = 0$ and $V_{\rm tv} = 1$ and

$$\delta V_{\rm rv} = F_{\rm vv}^2 s_{\rm vv} + F_{\rm hv}^2 s_{\rm hh}, \quad \text{copolar} \tag{15}$$

$$\delta V_{\rm rh} = F_{\rm hh} F_{\rm hv} s_{\rm hh} + F_{\rm vh} F_{\rm vv} s_{\rm vv} \quad \text{cross-polar} \tag{16}$$

The strongest terms are the first terms in the copolar receive channel and should dominate the second-order cross-polar terms (in general, $F_{\rm hv} \neq F_{\rm vh}$ [35]). The cross-polar terms given by (14) and (16) are first order in $F_{\rm hv}$ and $F_{\rm vh}$, and these terms set limits on how well radar can measure $s_{\rm hv}$, which is typically small for rain.

We can bring (13)–(16) into (5) and (6) to obtain the powers. Then, the bias of $Z_{\rm DR}$ in decibels is computed from

$$\begin{aligned} \text{bias}(Z_{\rm DR}) &\approx 10 \cdot \log(P_{\rm h}/P_{\rm v}) - Z_{\rm DR}^{\rm true} \\ &= 10 \cdot \log(B_4/B_5) - Z_{\rm DR}^{\rm true} \end{aligned} \tag{17}$$

where

$$\begin{aligned} B_4 &= \frac{\int_\Omega \left\langle |\delta V_{\rm h}|^2 \right\rangle d\Omega}{\left\langle |s_{\rm vv}|^2 \right\rangle} \\ &= \int_\Omega \left[Z_{\rm dr} |F_{\rm hh}|^4 + |F_{\rm vh}|^4 + 2\rho_{\rm hv} Z_{\rm dr}^{0.5} \text{Re}(e^{j\phi_{\rm dp}} F_{\rm hh}^{*2} F_{\rm vh}^2) \right] d\Omega \end{aligned} \tag{18}$$

$$\begin{aligned} B_5 &= \frac{\int_\Omega \left\langle |\delta V_{\rm v}|^2 \right\rangle d\Omega}{\left\langle |s_{\rm vv}|^2 \right\rangle} \\ &= \int_\Omega \left[|F_{\rm vv}|^4 + Z_{\rm dr} |F_{\rm hv}|^4 + 2\rho_{\rm hv} Z_{\rm dr}^{0.5} \text{Re}(e^{j\phi_{\rm dp}} F_{\rm vv}^2 F_{\rm hv}^{*2}) \right] d\Omega. \end{aligned} \tag{19}$$

The biases of $|\rho_{\rm hv}|$ and differential phase$\phi_{\rm dp}$ are given by

$$\text{bias}(|\rho_{\rm hv}|) = \frac{|\langle \delta V_{\rm h}^* \delta V_{\rm v} \rangle|}{\sqrt{\left\langle |\delta V_{\rm h}|^2 \right\rangle \left\langle |\delta V_{\rm v}|^2 \right\rangle}} - \left|\rho_{\rm hv}^{\rm true}\right| \tag{20a}$$

$$\text{bias}(\phi_{\rm dp}) = \text{angle}\left(\frac{\langle \delta V_{\rm rh}^* \delta V_{\rm rv} \rangle}{\sqrt{\left\langle |\delta V_{\rm rh}|^2 \right\rangle \left\langle |\delta V_{\rm rv}|^2 \right\rangle}} \right) - \phi_{\rm dp}^{\rm true} \tag{20b}$$

The biases of $|\rho_{\rm hv}|$ and differential phase $\phi_{\rm dp}$ can be re-written as

$$\text{bias}(|\rho_{\rm hv}|) = \frac{|B_6|}{\sqrt{B_4 B_5}} - \left|\rho_{\rm hv}^{\rm true}\right| \tag{21a}$$

$$\text{bias}(\phi_{\rm dp}) = \text{angle}\left(\frac{B_6}{\sqrt{B_4 B_5}} \right) - \phi_{\rm dp}^{\rm true} \tag{21b}$$

where B_4 and B_5 can be found in (18) and (19), respectively, and B_6 is

$$\begin{aligned} B_6 &= \frac{\int_\Omega \langle \delta V_{\rm h}^* \delta V_{\rm v} \rangle \, d\Omega}{\left\langle |s_{\rm vv}|^2 \right\rangle} \\ &= \int_\Omega \left[Z_{\rm dr} F_{\rm hh}^{*2} F_{\rm hv}^2 + F_{\rm vv}^2 F_{\rm vh}^{*2} + \rho_{\rm hv} e^{j\phi_{\rm dp}} Z_{\rm dr}^{0.5} F_{\rm hh}^{*2} F_{\rm vv}^2 \right. \\ &\qquad \left. + \rho_{\rm hv} e^{-j\phi_{\rm dp}} Z_{\rm dr}^{0.5} F_{\rm hv}^2 F_{\rm vh}^{*2} \right] d\Omega. \end{aligned} \tag{22}$$

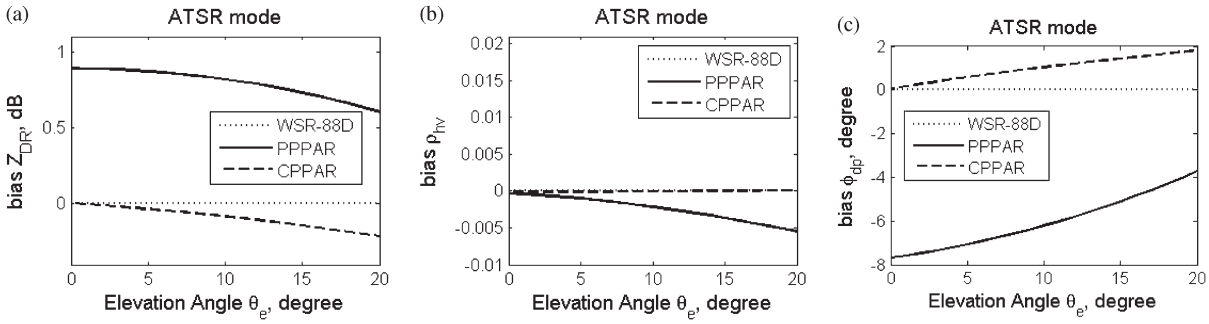

Fig. 9. Biases versus the beam's elevation angle $\theta_{\rm e}$ for the ATSR mode. $\rho_{\rm hv} = 0.90$, $Z_{dr} = 1$, and $\phi_{\rm dp} = 0$. The beam is pointed at $\phi_0 = 45°$, (a) $Z_{\rm DR}$ bias, (b) $\rho_{\rm hv}$ bias, and (c) $\phi_{\rm dp}$ bias.

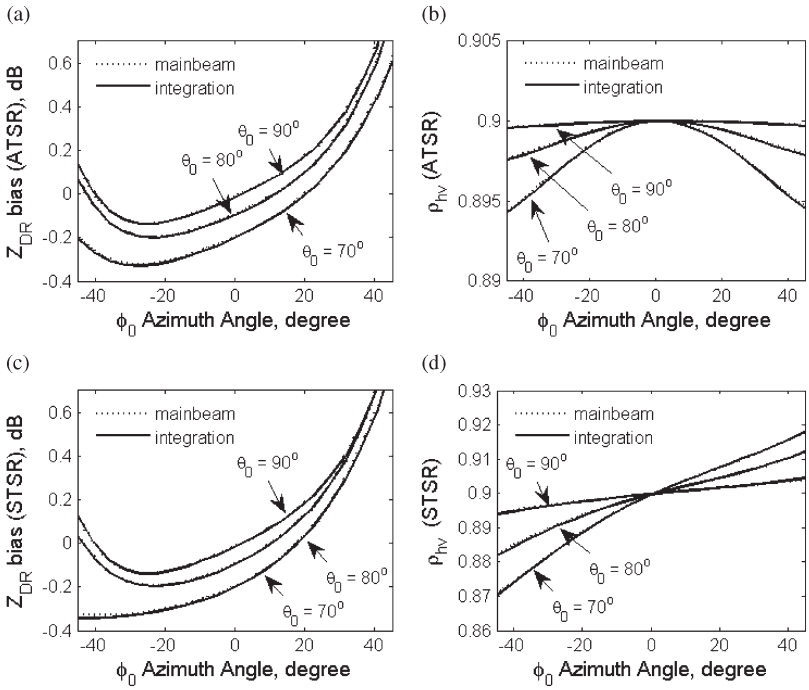

Fig. 10. $\rho_{\rm hv} = 0.90$, $Z_{\rm DR} = 1$ dB, and $\theta_o = 70°$ with main beam's (i.e., boresight) various azimuth angle. (a) $Z_{\rm DR}$ bias ATSR mode, (b) $\rho_{\rm hv}$ bias ATSR mode, (c) $Z_{\rm DR}$ bias STSR mode, and (d) $\rho_{\rm hv}$ bias STSR mode.

Fig. 9 shows the biases of $Z_{\rm DR}$, $\rho_{\rm hv}$, and $\phi_{\rm dp}$ as function of θ_e with $\phi_0 = 45°$ for the three antennas operating in the ATSR mode. Both the geometrically induced cross-polar bias and bias due to different gains in the H and V radiation patterns are added together in Fig. 9. CPPAR biases are much less than those of PPPAR.

C. Comparisons Between the Pattern Boresight Contribution and Integration

Lei *et al.* [15] and Zhang *et al.* [30] calculated the biases of polarimetric parameters of PPPAR considering only the boresight contribution of the radiation pattern (i.e., the effect of the entire copolar and cross-polar radiation patterns was ignored). In this section, we compare the biases from the boresight contributions and those biases calculated when the entire radiation patterns are integrated.

In order to obtain the integral contribution, the formulas in the previous section are used. The biases of polarimetric parameters considering only the boresight contribution of the patch antenna can be found in [15]. The patch element used in both calculations is the HFSS-simulated patch antenna patterns shown in Fig. 3. From Fig. 10, it is found that the results of integration contribution are very similar to the results of boresight contributions. These two only have a very slight difference. The reasons are that, for weather radar application, the beams are narrow, most power is located within the main lobe, and all sidelobes together contribute a relative small amount of power. Therefore, under these conditions, the simplified boresight formulas in [15], [30], and [33] can be used to calculate polarimetric parameter biases for PPPAR instead of using pattern integration formulas.

IV. Conclusion

The copolar and cross-polar radiation patterns and polarimetric parameter estimation performances of planar and cylindrical polarimetric phased array radars are studied and compared with that obtained using a dual-polarized parabolic reflector antenna (WSR-88D). By using the similar aperture size and

weighting, the normalized copolar patterns of phased arrays are almost the same as that of WSR-88D. However, for cross-polar patterns, three types of antenna have different properties. At broadside, all three antennas have a cross-polar pattern of 4-peak alternating phase symmetrically located about the copolar beam. The PPPAR radiation pattern evolves into a 1-peak cross-polar pattern coaxial with the copolar pattern which is the most effective in creating polarimetric parameter estimate bias as the beam scans away from principle planes. It is found that the cross-pol field of CPPAR is zero along the beam axis and the cross-pol peaks are much less than that of PPPAR.

Biases in the estimation of polarimetric variables, including differential reflectivity, correlation coefficient, and differential phase, are derived for both STSR and ATSR modes. Those formulas given in Section III are general formulas that apply to any type of antennas. The biases are calculated by the integration of the field in all directions assuming uniform reflectivity. For the mechanically steered parabolic reflector, there are no variations with direction, but for PPARs, the biases are functions of the beam scanning angle. Comparing CPPAR, PPPAR, and WSR-88D, it is found that biases of CPPAR are much less than those of PPPAR and biases of CPPAR are approaching the biases of WSR-88D.

For PPPAR, we compare the biases from the boresight contributions and those biases calculated when the entire radiation patterns are integrated and find that they are almost the same. For weather radar application, most power is located within the main lobe, and all sidelobes together contribute a relative small amount of power. Therefore, under these conditions, the simplified boresight formulas in [15], [30], and [31] can be used to calculate polarimetric parameter biases for PPPAR instead of using pattern integration formulas.

In this paper, the element effect is ignored for generality because the effect depends on a design of the antenna such as spacing, substrate materials, etc., and can be very different. Once an antenna design is specified, the antenna coupling effect can be studied using the embedded element patterns or the simulation for the full antenna array in the future work. What is more, the element pattern used in this paper is a simulation from a full-wave simulator. Measured antenna patterns can be used for more practical study. For CPPAR, the very low cross-polar patterns are due to the symmetrical arrangement of array elements. Any asymmetry of CPPAR will degrade the performance. Hence, the antenna element misalignment and asymmetry for CPPAR need further study.

Appendix A
Theoretical Far Field Copolar and Cross-Polar Radiation Patterns for the WSR-88D

Analytical solutions for the copolar electric field radiated by a circularly symmetric aperture distribution can be obtained from equations given in [23]. Applying these equations and normalizing, we obtain the theoretical pattern of copolar power density $S(u) = F_{\rm vv}^2(u)/g_{\rm vv}$

$$S(u) = 20\ \log_{10}\left[5.405\left|1.68\frac{4!J_4(u)}{u^4} + 0.16\frac{J_1(u)}{u}\right|\right] \tag{A1a}$$

where

$$u = \frac{2\pi\rho_o \sin\theta'}{\lambda},\ 2\rho_o = 8.534,\ \lambda(\text{KOUN}) = 0.1109\ \text{m} \tag{A.1b}$$

and θ', ϕ' are the polar and azimuth angles in the spherical coordinate system with the polar axis along the beam—because of symmetry, there is no ϕ' dependence for $F_{\rm vv}$.

Unfortunately, there is no analytical solution for the cross-polar $F_{\rm hv}$ of an axially symmetric aperture distribution. Thus, we use Jones' [13] theoretical formulas of the cross-polar far field of a reflector illuminated by a Hertzian dipole field to calculate the approximate angular distribution of cross-polar lobes, but the dipole's aperture field is multiplied by (1a) to account for the feed horn pattern weighting. Note that the $\rm TE_{11}$ distribution of the WSR-88D horn's radiation pattern partially cancels the cross-polar field generated by the reflector [10]. Thus, we cannot use the magnitude of the cross-polar field as calculated by Jones [13] to estimate the peak intensity of the cross-polar field. Cross-polar measurements are used to scale the theoretical cross-polar radiation patterns computed from Jones' formulas.

The integral for the far field cross-polar radiation field is given in [13, eq. (22)], and when $W(\rho)$ from (1a) is introduced, this equation becomes

$$E_{\rm x} = A\int_0^{\gamma} W(u)\frac{u^3 J_2(\beta u)\sin(2\phi')}{(1+u^2)^2}\,du \tag{A2}$$

where $E_{\rm x}$ is the cross-polar radiation in the far field, A is a normalizing constant, $u = \rho/2f$, $f = 3.2$ m is the focal length of KOUN's parabolic reflector, $\beta = 2kf\sin\theta'$ where $k = 2\pi/\lambda$, and J_2 is the Bessel function of the first kind of order 2. The azimuth angle ϕ' around the beam axis is referenced to the dipole's axis. This theoretical WSR-88D cross-polar pattern is plotted in Fig. 7(c) and is the one used to compute the polarimetric parameter biases for the WSR-88D. Also, plotted for comparison in Fig. 7(c) is the cross-polar pattern measured by Seavey Engineering on their antenna range in Massachusetts [2].

Appendix B
Transformation From Spherical Coordinates (r, θ', ϕ') of the Dish Antenna to the (r, θ, ϕ) Coordinates of Fig. 1.

See Fig. 11. XYZ is the dish antenna coordinate system, and the beam axis is along the X axis. (X, Y, Z) and (r, θ', ϕ') are related by $\begin{bmatrix} X \\ Y \\ Z \end{bmatrix} = \begin{bmatrix} r\sin\theta'\cos\phi' \\ r\sin\theta'\sin\phi' \\ r\cos\theta' \end{bmatrix}$. xyz is the coordinate system defined in Fig. 1. (x, y, z) and (r, θ, ϕ) are related by $\begin{bmatrix} x \\ y \\ z \end{bmatrix} = \begin{bmatrix} r\sin\theta\cos\phi \\ r\sin\theta\sin\phi \\ r\cos\theta \end{bmatrix}$. The relations of xyz and XYZ coordinates using Euler angles are derived as follows.

Let us first find the rotation angles between the xyz and the XY'Z' coordinate systems where Ox is in the XOY'plane (i.e., OY' is in the xoX plane). Initially, consider the XY'Z' coordinate systems to be overlapped with the xyz coordinate

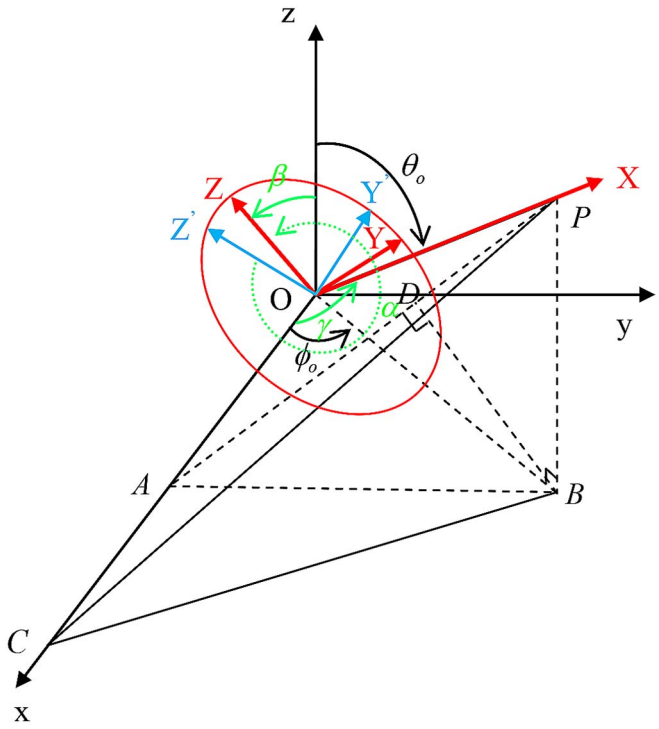

Fig. 11. Spherical coordinates (r, θ, ϕ) of Fig. 1 and the spherical coordinates (r, θ', ϕ') with the polar axis along the dish antenna's beam axis $X = r$.

system. First, rotate XY'Z' coordinates around the X axis by angle β. Then, rotate the XY'Z' coordinates around the Z' axis by the angle γ. After these rotations, OX is pointing to the (θ_o, ϕ_o) direction, and the rotation angles β and γ are calculated as now described. First, note that

$$\angle\text{POA} = \text{acos}\left(\frac{1 + (\sin\theta_o \cos\phi_o)^2 - \left[(\sin\theta_o \sin\phi_o)^2 + \cos^2\theta_o\right]}{|2\sin\theta_o \cos\phi_o|}\right) \tag{B1}$$

and assume that OP $= 1$, PB is perpendicular to the xOy plane, OP is perpendicular to PC, the PAB plane is perpendicular to the x axis, BD is perpendicular to PA, and D is on line PA. Then

$$AP = \sin(\angle\text{POA}) \tag{B2}$$

$$AB = \sin(\theta_o)\sin(\phi_o) \tag{B3}$$

$$PB = \cos(\theta_o) \tag{B4}$$

$$PC = \tan(\angle\text{POA}). \tag{B5}$$

It can be proved that PB is parallel to z and BD is parallel to Z. Therefore, β is equal to $\angle$PBD. Because $\angle$PBD is equal to $\angle$PAB, we finally find that β and γ are given by

$$\beta = \angle\text{PAB} = a\cos\left(\frac{AP^2 + AB^2 - PB^2}{2AP \cdot AB}\right) \tag{B6}$$

$$\gamma = \angle\text{POA} \tag{B7}$$

After the aforementioned two rotations, OX is along the (θ_o, ϕ_o) direction, but OY' is not parallel to the ground. Therefore, one more step of rotation is needed which is to rotate XY' Z' coordinates around the X axis by α degree to make OY' lines with OY which is in the plane of xoy. It can be proved that OY' is parallel to PC and OY is parallel to BC

$$\alpha = 360^\circ - \angle\text{PCB} = 360^\circ - a\tan(PB/PC). \tag{B8}$$

Therefore, for any point P, its coordinate system in xyz and XYZ is $[x_1, y_1, z_1]$ and $[X_1, Y_1, Z_1]$, respectively. Moreover, they are related by

$$\begin{bmatrix} X_1 \\ Y_1 \\ Z_1 \end{bmatrix} = \begin{bmatrix} 1 & 0 & 0 \\ 0 & \cos\alpha & \sin\alpha \\ 0 & -\sin\alpha & \cos\alpha \end{bmatrix} \begin{bmatrix} \cos\gamma & \sin\gamma & 0 \\ -\sin\gamma & \cos\gamma & 0 \\ 0 & 0 & 1 \end{bmatrix} \times \begin{bmatrix} 1 & 0 & 0 \\ 0 & \cos\beta & \sin\beta \\ 0 & -\sin\beta & \cos\beta \end{bmatrix} \begin{bmatrix} x_1 \\ y_1 \\ z_1 \end{bmatrix} \tag{B9}$$

where

$$\begin{bmatrix} X \\ Y \\ Z \end{bmatrix} = \begin{bmatrix} r\sin\theta'\cos\phi' \\ r\sin\theta'\sin\phi' \\ r\cos\theta' \end{bmatrix} \text{ and } \begin{bmatrix} x_1 \\ y_1 \\ z_1 \end{bmatrix} = \begin{bmatrix} r\sin\theta\cos\phi \\ r\sin\theta\sin\phi \\ r\cos\theta \end{bmatrix} \tag{B10}$$

REFERENCES

[1] C. A. Balanis, *Antenna Theory: Analysis and Design*, vol. xvi, 2nd ed. Hoboken, NJ, USA: Wiley, 1997.

[2] Baron, 2009 WSR-88D dual-polarization program, Report: Antenna component test, Baron Services, Inc., Huntsville, AL, USA, 2009.

[3] S. Bhardwaj and Y. Rahmat-Samii, "Revisiting the generation of cross-polarization in rectangular patch antennas: A near-field approach," *IEEE Antennas Propag. Mag.*, vol. 56, no. 1, pp. 14–38, Feb. 2014.

[4] E. A. Brandes, G. Zhang, and J. Vivekanandan, "Experiments in rainfall estimation with a polarimetric radar in a subtropical environment," *J. Appl. Meteorol.*, vol. 41, no. 6, pp. 674–685, Jun. 2002.

[5] V. N. Bringi *et al.*, "Design and performance characteristics of the new 8.5-m dual-offset Gregorian antenna for the CSU-CHILL radar," *J. Atmos. Ocean. Technol.*, vol. 28, pp. 907–920, Jul. 2011.

[6] G. E. Crain and D. Staiman, "Polarization selection for phased array weather radar," in *Proc. AMS 23rd Conf. IIPS Annu. Meet.*, San Antonio, TX, USA, Jan. 2007, pp. 1–9.

[7] D. T. Dawson, II, L. J. Wicker, E. R. Mansell, and R. L. Tanamachi, "Impact of the environmental low-level wind profile on ensemble forecasts of the 4 May 2007 Greensburg, Kansas, tornadic storm and associated mesocyclones," *Mon. Weather Rev.*, vol. 140, no. 2, pp. 696–716, Feb. 2012.

[8] R. Doviak *et al.*, "WSR-88D Radar for Research and Enhancement of Operations: Polarimetric Upgrades to Improve Rainfall Measurements," NOAA National Severe Storms Laboratory Report, Norman, OK, USA, p. 110, 1998. [Online]. Available: http://www.nssl.noaa.gov/publications/mpar_reports/

[9] Federal Aviation Admin., NextGen surveillance and weather radar capability, Washington, DC, USA, 2012.

[10] A. Z. Fradin, *Microwave Antennas*, New York, NY, USA: Pergamon, vol. 668, 1961.

[11] C. J. Fulton, "Digital array radar calibration and performance monitoring techniques for direct conversion and dual polarization architectures," Ph.D. dissertation, Purdue Univ., West Lafayette, IN, USA, 2011.

[12] M. Galletti and D. S. Zrnić, "Bias in copolar correlation coefficient caused by antenna radiation patterns," *IEEE Trans. Geosci. Remote Sens.*, vol. 49, no. 6, pp. 2274–2280, Jun. 2011.

[13] E. M. T. Jones, "Paraboloid reflector and hyperboloid lens antennas," *Trans. IRE Prof. Group Antennas Propag.*, vol. 2, no. 3, pp. 119–127, Jul. 1954.
[14] L. Josefsson and P. Persson, "Conformal array antenna theory and design," *IEEE Press Series on Electromagnetic Wave Theory*. New York, NY, USA: Wiley-IEEE Press, 2006, pp. 472–476, xiv, of plates ill. (some col.) 426 cm.
[15] L. Lei, Z. Guifu, and R. J. Doviak, "Bias correction for polarimetric phased-array radar with idealized aperture and patch antenna elements," *IEEE Trans. Geosci. Remote Sens.*, vol. 51, no. 1, pp. 473–486, Jan. 2011.
[16] H. Liu and V. Chandrasekar, "Classification of hydrometeors based on polarimetric radar measurements: Development of fuzzy logic and neuro-fuzzy systems, and in situ verification," *J. Atmos. Ocean. Technol.*, vol. 17, no. 2, pp. 140–164, Feb. 2000.
[17] A. Ludwig, "The definition of cross-polarization," *IEEE Trans. Antennas Propag.*, vol. 21, no. 1, pp. 116–119, Jan. 1973.
[18] V. M. Melnikov and D. S. Zrnić, "Simultaneous transmission mode for the polarimetric WSR-88D," NOAA National Severe Storms Laboratory Report, Norman, OK, USA, 2004. [Online]. Available: http://www.nssl.noaa.gov/publications/mpar_reports/
[19] Paramax, "Test report, antenna/pedestal, part 1 of 4, linear polarized antenna first article," U.S. Department of Commerce, Office of Procurement, Washington, DC, USA, 1992.
[20] H. S. Park, A. V. Ryzhkov, D. S. Zrnić, and K.-E. Kim, "The hydrometeor classification algorithm for the polarimetric WSR-88D: Description and application to an MCS," *Weather Forecast.*, vol. 24, no. 3, pp. 730–748, Jun. 2009.
[21] S. Perera *et al*., "A fully reconfigurable polarimetic phased array antenna testbed," *Int. J. Antennas Propag.*, vol. 2014, Article ID 439606 Aug. 2014.
[22] A. V. Ryzhkov, S. E. Giangrande, and T. J. Schuur, "Rainfall estimation with a polarimetric prototype of WSR-88D," *J. Appl. Meteorol.*, vol. 44, no. 4, pp. 502–515,Apr. 2005.
[23] J. W. Sherman and M. I. Skolnik, "Radar handbook," *in Aperture-Antenna Analysis*. New Year, NY, USA: McGraw-Hill, 1970, Ch. 9.
[24] M. Steiner and J. A. Smith, "Use of three-dimensional reflectivity structure for automated detection and removal of nonprecipitating echoes in radar data," *J. Atmos. Ocean. Technol.*, vol. 19, no. 5, pp. 673–686, May 2002.
[25] J. Vivekanandan *et al.*, "Cloud microphysics retrieval using S-band dual-polarization radar measurements," *Bull. Amer. Meteorol. Soc.*, vol. 80, no. 3, pp. 381–388, Mar. 1999.
[26] M. Weadon *et al.*, "Multifunction phased array radar," *Bull. Amer. Meteorol. Soc.*, vol. 90, pp. 385–389, 2009.
[27] M. E. Weber *et al.*, "The next-generation multimission U.S. surveillance radar network," *Bull. Amer. Meteorol. Soc.*, vol. 88, pp. 1739–1751, 2007.
[28] N. Yussouf, E. R. Mansell, L. J. Wicker, D. M. Wheatley, and D. J. Stensrud, "The ensemble Kalman filter analyses and forecasts of the 8 May 2003 Oklahoma City tornadic supercell storm using single- and double-moment microphysics schemes," *Mon. Weather Rev.*, vol. 141, no. 10, pp. 3388–3412, Oct. 2013.
[29] G. J. Vivekanandan and E. Brandes, "A method for estimating rain rate and drop size distribution from polarimetric radar measurements," *IEEE Trans. Geosci. Remote Sens.*, vol. 39, no. 4, pp. 830–841, Apr. 2001.
[30] G. Zhang *et al.*, "Phased array radar polarimetry for weather sensing: A theoretical formulation for bias corrections," *IEEE Trans. Geosci. Remote Sens.*, vol. 47, no. 11, pp. 3679–3689, Nov. 2009.
[31] G. Zhang *et al.*, "Polarimetric phased-array radar for weather measurement: A planar or cylindrical configuration?" *J. Atmos. Ocean. Technol.*, vol. 28, no. 1, pp. 63–73, Jan. 2011.
[32] D. A. S. Zrnić, A. Ryzhkov, J. Straka, Y. Liu, and J. Vivekanandan, "Testing a procedure for automatic classification of hydrometeor types," *J. Atmos. Ocean. Technol.*, vol. 18, no. 6, pp. 892–913, Jun. 2001.
[33] D. S. Zrnić, Z. Guifu, and R. J. Doviak, "Bias correction and Doppler measurement for polarimetric phased-array radar," *IEEE Trans. Geosci. Remote Sens.*, vol. 49, no. 2, pp. 843–853, Feb. 2011.
[34] D. S. Zrnić, R. J. Doviak, and V. M. Melnikov, "Issues and challenges for polarimetric measurement of weather with an agile beam phased array radar," NOAA National Severe Storms Lab., Norman, OK, USA, 2011. [Online]. Available: http://www.nssl.noaa.gov/publications/mpar_reports/
[35] D. S. Zrnić, R. J. Doviak, G. Zhang, and A. Ryzhkov, "Bias in differential reflectivity due to cross coupling through the radiation patterns of polarimetric weather radars," *J. Atmos. Ocean. Technol.*, vol. 27, no. 10, pp. 1624–1637, Oct. 2010.
[36] D. S. Zrnić, V. M. Melnikov, R. J. Doviak, and R. Palmer, "Scanning strategy for the multifunction phased-array radar to satisfy aviation and meteorological needs," *IEEE Geosci. Remote Sens. Lett.*, vol. 12, no. 6, pp. 1204–1208, Jun. 2015.
[37] D. S. Zrnić *et. al.*, "Agile-beam phased array radar for weather observations," *Bull. Amer. Meteorol. Soc.*, vol. 88, pp. 1753–1766, Nov. 2007.

Lei Lei received the Ph.D. and M.S. degree in electrical and computer engineering from the University of Oklahoma , Norman, OK, USA, in 2014 and 2009 respectively. She received B.S. degree in electrical engineering from Wuhan University, Wuhan, China, in 2006.

She was also a member of Atmospheric Radar Research Center (ARRC) of the University of Oklahoma. Currently, she works in Delphi Electronics and Safety, Kokomo IN, USA, as an Automobile Radar System Engineer. Her research interests include weather radar signal processing, weather radar polarimetry, phased arrays, automotive radar, and antenna design.

Guifu Zhang (S'97–M'98–SM'02) received the B.S. degree in physics from Anhui University, Anhui, China, in 1982, the M.S. degree in radio physics from Wuhan University, Wuhan, China, in 1985, and the Ph.D. degree in electrical engineering from the University of Washington, Seattle, WA, USA, in 1998.

From 1985 to 1993, he was an Assistant and Associate Professor in the Space Physics Department, Wuhan University. In 1989, he worked as a Visiting Scholar at the Communication Research Laboratory in Japan. From 1993 to 1998, he studied and worked in the Department of Electrical Engineering at the University of Washington, where he first was a Visiting Scientist and later a Ph.D. student. He was a Scientist with the National Center for Atmospheric Research during the period of 1998–2005. After that, he joined the School of Meteorology, University of Oklahoma, Norman, OK, USA, where he is now a Professor. He modeled and calculated wave scattering from fractal trees and that from a target buried under a rough surface. He explored the detection of targets in the presence of clutter using angular correlation functions. He developed algorithms for retrieving raindrop-size distributions. He led to develop advanced signal processing to improve weather radar data quality. He formulated the theory of weather radar interferometry and that of phased array radar polarimetry. His research interests include wave propagation and scattering in random and complex media, remote sensing theory and technology for geophysical applications, algorithms for retrieving physical states and processes, cloud and precipitation microphysics and model parameterization, target detection and classification, clutter identification and filtering, radar signal processing, and optimal estimation. He is currently interested in the design and development of polarimetric phased array radars for weather measurements and multimission capability.

Richard J. Doviak (S'56–M'57–SM'72–F'90–LF'97) received the B.S. degree in electrical engineering from Rensselear Polytechnic Institute, Troy, NY, USA, in 1956 and the M.Sc. and Ph.D. degrees from the University of Pennsylvania (UoP), Philadelphia, PA, USA, in 1959 and 1963, respectively.

He was Assistant Professor at UoP from 1963 to 1971, where he gave courses on electromagnetic theory, wave propagation, and scattering in turbulent media. During 1967–1971, he was a Principal Investigator (PI) of UoP's Valley Forge Research Center in a joint experiment with scientists from the Johns Hopkins Applied Physics Laboratory to measure forward scatter from the cloudless troposphere. He joined the National Severe Storms Laboratory (NSSL), National Oceanic and Atmospheric Administration, Norman, OK, USA, where he headed the Doppler Radar Project (1971–1987). He was a PI (1983–1986) of the National Aeronautics and Space Administration funded research at the University of Oklahoma to map wind, waves, and turbulence with an airborne Doppler lidar. He was a Visiting Professor (1987) at the Kyoto University, Japan, where he lectured on Doppler weather radar, and was an Affiliated Scientist (1992–2000) at the National Center for Atmospheric Research, Boulder, CO, USA. He is currently a Senior Engineer at NSSL and an Affiliated Professor with the School of Electrical and Computer Engineering and the School of Meteorology, University of Oklahoma in Norman, OK, USA. He is the coauthor of the text "Doppler Radar and Weather Observations."

Dr. Doviak was a Guest Editor for a Special Issue of the IEEE TRANSACTIONS ON GEOSCIENCE AND REMOTE SENSING (TGARS, 1979) on the subject of Radio Meteorology, an Associate Editor for the American Meteorological Society's (AMS) journals of *Atmospheric and Oceanic Technology* (1984–1988) and *Applied Meteorology* (1977–1980), and an Editor of TGARS (1988–1991). He was a recipient of IEEE's Harry Diamond Memorial Award in 1988 for his outstanding technical contributions in the field of government services in any country. He is a Fellow of the AMS and the Cooperative Institute of Mesoscale Meteorological Studies of the University of Oklahoma, Norman, OK, USA. He has given short courses on Radar Meteorology at the U.S. National Radar Conferences and at the AMS Annual meetings.

Shaya Karimkashi (S'08–M'11) received the B.S. degree electrical engineering from the K. N. Toosi University of Technology, Tehran, Iran, in 2003, the M.S. degree electrical engineering from the University of Tehran, Tehran, in 2006, and the Ph.D. degree electrical engineering from the University of Mississippi, University, MS, USA, in 2011.

He joined the Advanced Radar Research Center at the University of Oklahoma, Norman, OK, USA, in 2011, where he is currently a Research Scientist and an Adjunct Assistant Professor. He has published over 30 referred journal and conference papers. His research interests include the area of antenna arrays, polarimetric phased array radars, focused antennas, computer-aided design for antennas, and optimization techniques in electromagnetics.

Dr. Karimkashi is a member of the IEEE Antennas and Propagation, Phi Kappa Phi, and Sigma Xi societies.